

Smart Tissue Anastomosis Robot (STAR): Accuracy Evaluation for Supervisory Suturing Using Near-Infrared Fluorescent Markers

Simon Leonard, Azad Shademan, Yonjae Kim, Axel Krieger and Peter C. W. Kim

Abstract—This paper specifies and evaluates the accuracy of the Smart Tissue Anastomosis Robot (STAR). The STAR is a proof of concept vision-guided robotic system equipped with an actuated laparoscopic suturing tool and a multispectral vision system. The STAR supports image-based suturing commands and is capable of detecting near-infrared fluorescent (NIRF) markers that provide reliable visual segmentation and tracking. The paper reports the best case scenario accuracy specifications of the STAR as derived from its configuration and calibration parameters. We also evaluate experimentally the effects of overlaying NIRF markers on the accuracy of the STAR when these markers are used as the source of image-based commands and we compare these results to the accuracy of the STAR with image-based commands generated from plain color images. Our results demonstrate that the STAR is able to place sutures on a planar phantom with an average accuracy of 0.5 mm with a standard deviation of 0.2 mm and that NIRF markers have no statistically significant adverse effect on the accuracy.

I. INTRODUCTION

Robotic assisted surgeries (RAS) have significantly improved the ergonomics for surgeons and contributed to faster recoveries and shorter hospitalizations for patients. Despite this progress, one of the most time-consuming and repetitive stages during a laparoscopic surgery remains the suturing or stapling of surgical incisions such as anastomoses. The average duration for a RAS laparoscopic anastomosis ranges from 30 to 90 minutes for intestinal [1] and 28 minutes for vascular [2]. Thus, the motivations to partially or fully automate laparoscopic suturing are 1) the low suturing efficiency of current surgical robots and 2) the variability of procedural techniques between surgeons affects the consistency of validated metrics for anastomosis such as bursting strength and accuracy [3].

Several surgical robots have proposed to automate laparoscopic suturing but the challenges of sensing and tracking tissues in a surgical environment have prevented most of them from reaching clinical stages. These challenges mainly stem from the poor visibility of the tissues, occlusions, specularities and non-rigid deformations. Whereas several RAS systems address these challenges by augmenting or complementing human perception [4] or motor skills [5], the Smart Tissue Anastomosis Robot (STAR) [6] aims to substitute the motor skills of surgeons and sensing by using actuated tools and sensing that are designed to address challenges of laparoscopic suturing. To address the challenges of tissue sensing and tracking that are inherent to surgeries, the STAR uses near-infrared fluorescent (NIRF) markers in



(a) STAR system. (b) Circular needle of the Endo360°.

Fig. 1. a) The STAR hardware: A 7 DOF LWR mounted with an modified Endo360°. b) The actuated needle of the STAR.

combination with a multispectral vision system that is capable of segmenting the markers reliably despite occlusions and overlaying them on intraoperative color images. This is possible because NIRF light penetrates through blood and tissue. These markers are placed by a surgeon at the desired stitching sites and the markers are segmented and tracked by the vision system to guide the motion of the robot.

The first contribution of this paper is to derive the open-loop accuracy specifications of the STAR in a non-clinical environment. These specifications are used to determine which suturing tasks could be executed by the STAR and to establish a baseline for more realistic experiments. The second contribution is to evaluate the accuracy of the STAR with and without NIRF markers and to determine if the accuracy is within the specified bounds. Finally, we answer the question as to whether the NIRF markers affect the STAR accuracy in our experiments.

The main components of the STAR are a robot arm equipped with an actuated suturing tool and a multispectral vision system (Fig. 1a). The STAR tool is an actuated version of the Endo360°[®] (EndoEvolution, North Chelmsford, MA) that is mounted on a 7 degrees of freedom (DOF) Light Weight Robot (LWR) from Kuka (Kuka AG, Augsburg Germany). The tool has two actuators, one to drive a circular needle and one to drive the pitch axis located 46 mm above the tip of the tool as illustrated in Fig. 1b. The multispectral vision system enables to visualize intraoperative color and infrared images. Infrared images are used to enhance visual tracking by segmenting NIRF markers that can be segmented when occluded by up to 2 mm of tissues [7]. The color images are used to manually select the image coordinates of each stitch and these coordinates are transformed to 3D suturing commands to the robot that plans and executes the

The authors are with the Sheikh Zayed Institute for Pediatric Surgical Innovation at the Children's National Medical Center, Washington DC

motion.

II. PREVIOUS WORK

The field of robotic assisted surgeries includes a broad range of applications including orthopedics, neurology, urology, ocular and general surgeries. In the case of minimally invasive surgeries (MIS), one important challenge is to work in a confined space under the constraints imposed by the tools insertion points. Robotic systems such as the da Vinci Surgical System [8], Raven [9] and MiroSurge [10] are teleoperated MIS robots that provide surgeons with a greater dexterous workspace and improved visualization when compared to manual laparoscopic instruments. It is important to underline, however, that the purpose of these systems is to enhance the skills of surgeons as opposed to fully or partially automate a surgical procedure or part thereof. Previous research has demonstrated the benefits of actively modifying the motion of these robots according to a specified task or constraints. One example involve a system capable to segment a surgeon's motion during a suturing task with a da Vinci [11] and to synchronize a similar motion segment recorded by an expert. Various systems have proposed to combine haptic feedback with virtual fixtures [12] to guide the motion of the surgeon along a path in the workspace [13], [14] or to prevent the end-effector from entering specific areas [15].

A different paradigm for RAS consists of shifting a greater portion of autonomy on the robot system, sensors and controllers. Several laparoscopic hand-held tools for suturing or knot tying have been designed [16], [17], [18], [19] and some master-slave robots provide features for suturing such as force feedback [20], programmable modes [21] and virtual fixture for tool alignment [13]. None of these systems, however, are able to close an incision without a "surgeon in the loop". Recently, a single arm robot equipped with a laparoscopic needle holder demonstrated it could insert a needle in a phantom by using circular markers [22]. The accuracy criteria, however, consisted of successfully inserting the needle within 3 mm surface markers and the results varied according to light intensity. The STAR proposes a similar supervised control approach that shifts the burden of planning and executing the motion on the robotic system while maintaining the role of the surgeon to decide where to place each suture. The STAR, however, combines a specialized suturing tool with vision system that enables to reliably segment and track NIRF markers.

III. SMART TISSUE ANASTOMOSIS ROBOT

The STAR system is a combination of robot hardware, multispectral imaging and control software. In this paper we report the accuracy of the STAR for suturing on a planar phantom. Although a planar phantom represents a significant assumption for any surgical task, similar conditions have been reported in the literature for systems in the pre-clinical development phase [13], [18], [22], [23], [24]. Furthermore, given that this paper aims to evaluate the accuracy of the STAR in a non-clinical environment, a

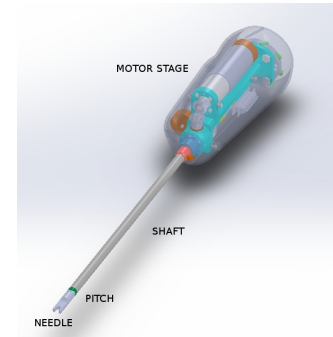


Fig. 2. Computer-aided design of the STAR tool.

planar phantom provides a reliable ground truth that enables accurate measurements of non-biomechanical parameters.

A. Actuated Suturing Tool

We designed and built a single degree-of-freedom suturing stage, motorizing pitch and needle actuation of a commercially available manual suture tool Endo360°. Fig. 2 shows a computer aided design (CAD) drawing of the automated suturing tool design. The manual Endo360° tool is able to drive a disposable suture needle with attached 3-0 suture along a circular path, enabling single handed laparoscopic suturing. The manual handle of the Endo360° was disconnected and the tool head, tool shaft, cables to actuate needle drive and push-pull bar to actuate pitch were connected to an aluminum bracket. Two DC brush motors (Maxon Motors, Sachseln, Switzerland) drive pitch and needle actuation through two bevel gears activating a cam drive for pitch actuation and a bidirectional cable drive with pulley for needle actuation. Two turnbuckles allow for adjusting the tension of the cables for the needle actuation. Epos 2 (Maxon Motors, Sachseln, Switzerland) controllers are used for motor control.

B. Near Infrared Fluorescence Imaging (NIRF)

NIRF imaging is a technique that uses the near-infrared (NIR) wavelengths of the light spectrum (700 – 1000 nm) to excite a fluorophore agent, which emits its excited photons in the NIR wavelengths. Excited photons propagate and penetrate soft tissue, enabling better signal-to-noise ratios in poor visible-light conditions. NIRF imaging has been successfully used for several biomedical imaging applications. The main application has been oncology and the intraoperative visualization of cancer cells during surgery [25]. The field of NIRF is rapidly growing and there has been recent examples of its application in intraoperative image-guided surgery [26], [25].

We developed a NIRF imaging system to be used for supervisory suturing by a surgeon via a graphical user interface. The proposed imaging system consists of a high power light-emitting diode (LED) light source acting as the NIRF excitation light, a NIR camera with emission filter to capture the emitted NIR light, and a color camera to capture the visible-light scene. The excitation light is a custom-built eight-LED ring light with narrow-band high-power 760 nm LEDs (North Coast Technical Inc., Chesterland, OH). The wavelength is chosen according to the peak absorption

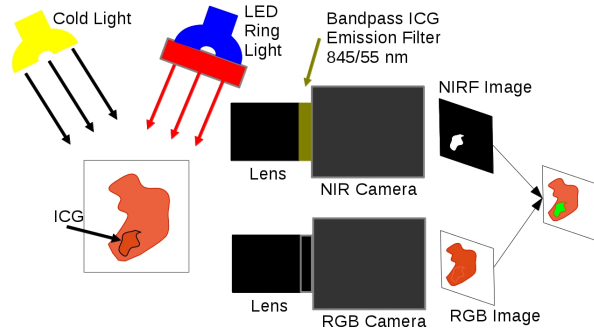


Fig. 3. NIRF Imaging System Diagram.

wavelength of the fluorophore. The NIRF imaging sensor is an acA-50gm 2000NIR gigabit Ethernet (GigE) camera (Basler Inc., Exton, PA) equipped with the NIR-enhanced CMOSIS CMV2000 2048 × 1088 pixel CMOS sensor and a bandpass 845nm ± 55nm filter (Chroma Technology Corp., Bellows Falls, VT). The color image is captured with a 1288 × 964 Flea2 camera (Point Grey Research, Richmond, BC) with a color (RGB) Sony ICX445 sensor. Both cameras use Tamron 23FM08-L lenses with focal length of 8 mm. A diagram of our NIRF imaging system is depicted in Fig. 3.

A typical fluorophore, which re-emits light upon infrared light excitation, is indocyanine green (ICG). We have previously developed NIRF markers based on the ICG [7]. The details of the NIRF marker preparation and a feasibility study of its applicability for visual tracking is studied in our previous work [7].

The NIRF marker is delivered with a 20 μl Biohit Proline Mechanical Pipette, which allows delivery of small droplets of ICG on the accuracy handle (see Fig. 4, and 7).

C. Supervisory Control

As described in Section II, several RAS systems are designed around the master-slave or shared control paradigms that enable a surgeon to directly control the motion of a robot. The STAR system is built around the supervisory control paradigm that enables a surgeon to specify high level suture commands and leave the details of implementing the suturing motion to the robotic system. As presented in Section III-B, the current version of the STAR provides multispectral intraoperative images that overlays segmented NIRF markers on the RGB images. Using a computer input device, a surgeon generates image-based suture commands by selecting the markers in a desired order. As illustrated in Fig. 4, however, the segmented NIRF markers used in our experiments are not consistent and some have a larger size than others. This is caused by a range of factors including the volume of the ICG deposit, the amount of light it receives and the diffusion caused by surrounding tissues. It is thus important to evaluate the effect, if any, of these markers on the STAR accuracy and if they can be used reliably for vision-based guidance. Several parameters must be considered to determine the 3D suturing accuracy of the STAR. First, kinematics errors result from possible errors in the model of the LWR, misalignment between the laparoscopic tool shaft and the LWR flange and errors in position of

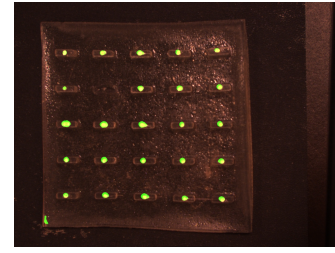


Fig. 4. NIR markers are segmented from the NIR camera and overlaid on top of the RGB image. The empty slot in the second row is caused by a damage to the pad and not caused by a lack of fluorescence.

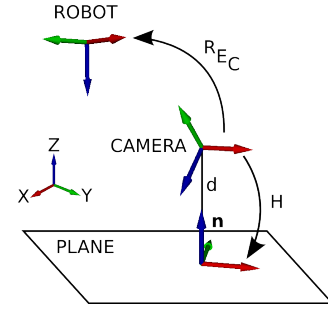


Fig. 5. Schematic drawing of coordinate frames. X axes are in red, Y axes are in green and Z axes are in blue. The plane normal n corresponds to the Z axis of the plane.

the tool pitch axis. Second, hand-eye calibration and camera calibration errors result in errors in robot commands. Third, the manual selection of a selected 3D point can result in errors of several pixels. Although we concede that kinematics errors are unavoidable, we carefully assessed the kinematics calibration of the LWR during the hand-eye calibration. The measured deviation of the tool was in the order of 0.1mm which is significantly smaller than errors from the hand-eye calibration and selection errors and was therefore discarded.

Several relationships must be determined in order to move the tool control point (TCP) to a 3D position that corresponds to a selected image point and these relationships are subject to measurement errors. Given the planar surface of the phantom, the homography between the suturing plane and the image plane must be known and the transformation between the cameras and the robot must also be known. As illustrated in Fig. 5, the homography H between the suturing and image planes does not constrain the origin of the coordinate frame of the suturing plane and it does not constrain the orientation of the plane about its normal axis. Thus, we impose the relative orientation between the suturing plane and the color camera to have zero rotation about Z such that the orientation of the plane only requires rotations about X and Y axes. Errors resulting from camera calibration are available from the camera parameters and the reprojection errors. Let K define a camera projection matrix

$$K = \begin{bmatrix} f_x & 0 & c_x \\ 0 & f_y & c_y \\ 0 & 0 & 1 \end{bmatrix} \quad (1)$$

where $f_x = s_x f$ and $f_y = s_y f$ are the scaled focal length and

c_x and c_y are the coordinates of the optical center. Let

$${}^C E_P = \begin{bmatrix} \mathbf{r}_1 & \mathbf{r}_2 & \mathbf{r}_3 & \mathbf{t} \\ 0 & 0 & 0 & 1 \end{bmatrix} \quad (2)$$

where \mathbf{r}_1 , \mathbf{r}_2 and \mathbf{r}_3 are columns of a rotation matrix and \mathbf{t} is a translation vector that define the rigid transformation of the suturing plane P with respect to the camera coordinate frame C as illustrated in Fig. 5. A point on the suturing plane is defined by the coordinates ${}^P \mathbf{P} = [{}^P X \ {}^P Y \ 0]^T$ and is projected to an image point with homogeneous coordinates $\mathbf{p} = [x \ y \ 1]^T$ according to a homography

$$\mathbf{p} \sim H [{}^P X \ {}^P Y \ 1]^T, \quad (3)$$

where H is defined up to a scale by

$$H = K [\mathbf{r}_1 \ \mathbf{r}_2 \ \mathbf{t}]. \quad (4)$$

If H is non-singular, the coordinates ${}^P X$ and ${}^P Y$ are determined by

$$w [{}^P X \ {}^P Y \ 1]^T = H^{-1} \mathbf{p} \quad (5)$$

where w is the scale factor. Furthermore, ${}^P \mathbf{P}$ is transformed to a 3D point in the coordinate system of the camera by

$${}^C \mathbf{P} = {}^C E_P [{}^P X \ {}^P Y \ 0 \ 1]^T. \quad (6)$$

We define the suturing plane normal by \mathbf{n} and the distance between the color camera and the suturing plane by d . Substituting Equation (5) in (6) (taking care of normalizing the homogeneous coordinates) we obtain that the 3D camera coordinates of an image point \mathbf{p} are given by

$${}^C \mathbf{P} = \frac{d}{\mathbf{n}^T [f_y(x-c_x) \ f_x(y-c_y) \ f_x f_y]^T} \begin{bmatrix} f_y(c_x - x) \\ f_x(c_y - y) \\ -f_x f_y \end{bmatrix}. \quad (7)$$

Given that we constrain the orientation of the plane with respect to the camera, we note that $\mathbf{n} = [\sin(\alpha) \ -\sin(\alpha)\cos(\beta) \ \cos(\alpha)\cos(\beta)]^T$, where α and β are the rotation angles about X and Y respectively and $d = -\mathbf{n}^T \mathbf{t}$.

Once the ${}^C \mathbf{P}$ is computed, the coordinates are transformed in the coordinate system of the robot with

$${}^R \mathbf{P} = {}^R E_C {}^C \mathbf{P}. \quad (8)$$

According to Equation (7), the coordinates of a point in the camera frame depend on the following nine parameters: five extrinsic camera parameters, four intrinsic camera parameters and two image coordinates. Given the non-linear nature of Equation (7), if

$$\mathbf{X} = [\mathbf{t}^T \ \alpha \ \beta \ f_x \ f_y \ c_x \ c_y \ x \ y]^T$$

designates a random vector of the parameters with expected value $\bar{\mathbf{X}}$ and covariance $\Sigma_{\mathbf{X}}$, the covariance of a 3D point in the camera coordinate frame is given by $\Sigma_{\mathbf{P}} = J_{\bar{\mathbf{X}}} \Sigma_{\mathbf{X}} J_{\bar{\mathbf{X}}}^T$ where $J_{\bar{\mathbf{X}}}$ is the Jacobian of partial derivatives $\partial {}^C \mathbf{P} / \partial \mathbf{X}$ evaluated at $\bar{\mathbf{X}}$.

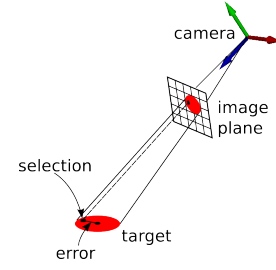


Fig. 6. Error from placement selection is used to estimate the selection covariance $\Sigma_{selection}$

We decompose the 11×11 matrix $\Sigma_{\mathbf{X}}$ in the following block diagonal

$$\Sigma_{\mathbf{X}} = \begin{bmatrix} \Sigma_{camera} & 0 \\ 0 & \Sigma_{selection} \end{bmatrix}$$

where $\Sigma_{camera} = (J_C^T \Sigma_{points}^{-1} J_C)^{-1}$ is the 9×9 covariance of the estimated camera, where J_C is a $N \times 9$ camera Jacobian that is evaluated from N measured points as described in [27] and $\Sigma_{selection}$ is the 2×2 covariance caused by errors in the selection of a placement as illustrated in Fig. 6. Given a spherical marker with radius r and 3D coordinates ${}^P \mathbf{P}$, the covariance $\Sigma_{selection}$ captures the error in selecting a pixel that does not correspond to the center of the marker. Thus, although $\Sigma_{selection}$ can be arbitrarily large, it determines how accurate a surgeon must be in selecting a placement to achieve a desired accuracy given a hand-eye configuration.

Likewise, the covariance resulting from estimating the hand-eye calibration transformation ${}^R E_C$ is determined from residuals during the calibration procedure. The STAR is configured as an eye-to-hand system where the camera is static and observes the tip of the robot laparoscopic tool. Because of this configuration, our hand-eye calibration procedure involves mounting a calibration rod on the robot and moving the TCP to a few positions on a calibrating pattern that is registered in the camera coordinate system. Using a set of N measurements ${}^P \mathbf{P}_i$ ($1 \leq i \leq N$) in the robot coordinate system and the corresponding measurements ${}^C \mathbf{P}_i$ in the camera coordinate system, we use the standard least-squares method presented in [28] to estimate the transformation ${}^R E_C$. Using the errors resulting from this registration we estimate the hand-eye covariance $\Sigma_{handeye} = J_H \Sigma_H J_H^T$ where J_H is the Jacobian between the camera and robot frames and Σ_H is the covariance of measured errors.

IV. EXPERIMENTS

We first performed a full calibration of the STAR from which the accuracy specifications are derived. Then, we performed two sets of experiments, one with NIRF markers and one without, to validate the accuracy of the STAR and to compare these results to the specifications. The LWR manipulator is mounted upside down on the ceiling facing an operating room table. Given that the STAR tool overall length measures 680 mm, the height of the table was adjusted at 1.7 m below the base of the robot to enable the tool control point to reach the table while avoiding full extension. The cameras were mounted side by side looking down with their

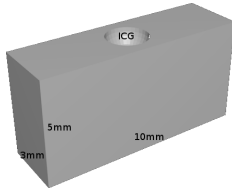


Fig. 7. Handle used to measure STAR accuracy.

optical axis slightly looking down the $-Y$ axis of the robot base. The RGB camera, which is used as the main video source, framed an area of 12×10 cm of the table (see Fig. 4 for a typical view).

We molded gelatin suturing pads to measure the accuracy of the STAR. Each pad provides 25 suturing handles each of size $10 \times 3 \times 5$ mm that are distributed evenly on a 10×10 cm flat surface (see Fig. 4). For the NIRF markers experiment, the top surface of each handle contains a recessed hemisphere of 1 mm radius that is able to contain roughly $15 \mu\text{L}$ of ICG as illustrated in Fig. 7.

A. Theoretical Accuracy Specifications

The images from the RGB camera were selected as the main video source for the user interface. The main motivation for this decision is the better calibration of the RGB camera compared to the NIR camera. Thus, only image points from the RGB camera are used to specify suture commands and, therefore, only the parameters of the RGB camera are relevant to estimate the accuracy of the STAR.

The calibration of the RGB camera was validated with a calibration pattern and the root mean square (RMS) reprojection error was 0.2 pixel. This error was used to generate the covariance matrix Σ_{points} and, along with the Jacobian J_C also derived from the calibration validation, was used to evaluate Σ_{camera} .

The covariance $\Sigma_{\text{selection}}$ for selection errors was set to 5 pixels for both horizontal and vertical image coordinates. This value roughly corresponds to average radius of the projected markers in the image.

The hand-eye calibration procedure was described in Section III-C. The procedure involves using the robot to touch a few fiducial points on a calibration pattern and then estimate the rigid transformation between the 3D coordinates measured with the robot and those measured with the calibrated RGB camera. The hand-eye calibration resulted in a RMS error of 0.23 mm. During the hand-eye calibration we also validated the kinematics deviations of the STAR by ensuring that the relative motion between each position was consistent with those on the calibration pattern. The deviation of the tool was measured at 0.1 mm and was neglected.

Using the covariance Σ_{camera} and $\Sigma_{\text{selection}}$, the 11×11 covariance matrix Σ_X is computed and then converted to the 3D covariance matrix Σ_P with the Jacobian $J_{\hat{X}}$. Finally, Σ_P , which represents the uncertainty of the 3D coordinates in the camera coordinate frame, is converted to the covariance matrix Σ_H which represents the uncertainty of the 3D coordinates in the robot frame. A matrix Σ_H was computed for each image coordinate in the RGB camera and the average errors are reported in Table I.

TABLE I

THEORETICAL AVERAGE ERRORS AND STANDARD DEVIATIONS

$\mu_X(\sigma_X)$	$\mu_Y(\sigma_Y)$	$\mu_Z(\sigma_Z)$
1.4 mm (0.1 mm)	0.8 mm (0.1 mm)	1.0 mm (0.2 mm)

TABLE II

MEASURED AVERAGE ERRORS AND STANDARD DEVIATIONS

Red Markers	NIRF Markers
0.4567 mm (0.1495 mm)	0.4721 mm (0.1695 mm)

We observe that the deviation along X is greater than the deviation along Y . This is explained by the orientation of the camera with respect to the robot where the optical axis of the camera was slightly aligned with the X axis of the robot.

B. Ink Markers

In our first experiment we only used RGB images to determine the stitches placements. We used a red marker to draw a small dot (roughly 1 mm radius) on the top surface of each handle which resulted in dots of about 6 pixels radius in the RGB images. The images were displayed on a computer screen and the placement of each stitch was selected by manually clicking in the middle of each dot. Each mouse click was transformed to the coordinate system of the robot using Equations (8) and (7). Given that the kinematics of the STAR tool accounts for the needle tip, 1.5 mm was added to the Z coordinate to enable the needle to bite the gelatin. The normal orientation of the TCP was aligned opposite to the normal of the plane.

The error of each suture was determined by measuring the distance with a caliper between the thread and the center of the marker while looking through the gelatin as shown in Fig. 8. The mean error and standard deviation for this experiment are reported in Table II and are within the margins of confidence reported in Table I.

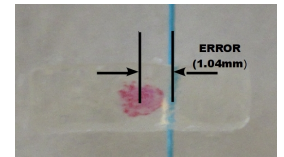


Fig. 8. Measurement of error for each handle.

C. NIRF Markers

We repeated the previous experiment by replacing the ink dots with NIRF markers. A small dose of ICG was dropped into the cavity on the surface of each handle by using a single channel micropipette. The NIR light source was placed above the suturing plane and the markers were segmented with image processing algorithms consisting of histogram equalization, morphological operations and thresholding. The resulting binary image was overlayed on the color image by means of a homography which maps the view of the suturing plane in the NIR images onto the view of the suturing plane in the color images. The homography was computed during the calibration of the cameras.

After the completion of the suturing, we measured the error between the center of the hemispheres and the thread. The mean error and standard deviation for this experiment are reported in Table II and are also within the margins of confidence reported in Table I.

To determine if the NIRF markers affect the accuracy error we tested the hypothesis that the mean error when using NIRF markers is equal to the mean error without using NIRF markers by performing two-sample t-test. The test result $p = 0.7397$ suggests that NIRF markers did not have a significant impact on the the accuracy of the STAR.

V. CONCLUSION AND FUTURE WORK

The STAR aims to relieve a surgeon from the burden of manual suturing by partially automating laparoscopic suturing. The system combines a robot arm with an actuated suturing tool totalling 8 DOF with vision-guidance to enable a surgeon to place stitches by selecting them from intraoperative images. The STAR also provides multispectral imaging to segment and track NIRF markers that are placed on the surface of tissues. This paper reports the accuracy specifications of the STAR and evaluates its accuracy in practice by measuring the errors at several positions on a planar phantom. Our experiments demonstrate that the accuracy of the STAR is less than 0.5 mm and is within the expected specifications. We also demonstrate that accuracy of the STAR is not affected by NIRF markers and its accuracy remains within the specifications. We are currently in the process of extending the capabilities of the STAR to suture 3D structures by replacing the RGB camera with a light-field camera and by developing an actuated stapling tool.

ACKNOWLEDGEMENTS

The authors would like to thank Dr. Matthieu F. Dumont for preparing the ICG fluorophore.

REFERENCES

- [1] J. Ruurda, I. Broeders, B. Pulles, F. Kappelhof, and C. van der Werken, "Manual robot assisted endoscopic suturing - Time-action analysis in an experimental model," *Surgical Endoscopy And Other Interventional Techniques*, vol. 18, no. 8, pp. 1249–1252, August 2004.
- [2] P. Štádlér, L. Dvořáček, P. Vitásek, and P. Matouš, "The application of robotic surgery in vascular medicine," *Innovations*, vol. 7, no. 4, pp. 247–253, 2012.
- [3] M. Waseda, N. Inaki, J. R. T. Bermudez, G. Manukyan, I. A. Gacek, M. O. Schurr, M. Braun, and G. F. Buess, "Precision in stitches: Radius surgical system," *Surgical Endoscopy*, vol. 21, no. 11, pp. 2056–2062, November 2007.
- [4] K. K. Badani, A. Bhandari, A. Tewari, and M. Menon, "Comparison of two-dimensional and three-dimensional suturing: Is there a difference in a robotic surgery setting?" *Journal of Endourology*, vol. 9, December 2005.
- [5] D. Nio, R. Balm, S. Maartense, M. Guijt, and W. A. Bemelman, "The efficacy of robot-assisted versus conventional laparoscopic vascular anastomoses in an experimental model," *European Journal of Vascular and Endovascular Surgery*, vol. 27, pp. 283–286, 2004.
- [6] S. Leonard, K. L. Wu, Y. Kim, A. Krieger, and P. C. Kim, "Smart tissue anastomosis robot (STAR): A vision-guided robotics system for laparoscopic suturing," *IEEE Transactions on Biomedical Engineering*, Preprint.
- [7] A. Shademan, M. F. Dumont, S. Leonard, A. Krieger, and P. C. W. Kim, "Feasibility of near-infrared markers for guiding surgical robots," in *SPIE Proceedings Vol. 8840 Optical Modeling and Performance Predictions VI*, vol. 8840, 2013.
- [8] G. T. Sung and I. S. Gill, "Robotic laparoscopic surgery: a comparison of the da vinci and zeus systems," *Urology*, vol. 58, no. 6, p. 893898, December 2001.
- [9] J. Rosen and M. Hannaford, "Doc at a distance," *IEEE Spectrum*, pp. 34–39, October 2006.
- [10] U. Hagn, R. Konietzschke, A. Tobergte, M. Nickl, S. Jrg, B. Kbler, G. Passig, M. Grger, F. Frhlich, U. Seibold, L. Le-Tien, A. Albuschffer, A. Nothhelfer, F. Hacker, M. Grebenstein, and G. Hirzinger, "DLR MiroSurge: a versatile system for research in endoscopic telesurgery," *International Journal of Computer Assisted Radiology and Surgery*, vol. 5, pp. 183–193, March 2010.
- [11] H. C. Lin, I. Shafran, D. Yuh, and G. D. Hager, "Towards automatic skill evaluation: Detection and segmentation of robot-assisted surgical motions," *Computer Aided Surgery*, vol. 11, no. 5, pp. 220–230, 2006.
- [12] J. J. Abbott, P. Marayong, and A. M. Okamura, "Haptic virtual fixtures for robot-assisted manipulation," *Robotic Research*, vol. 28, pp. 49–64, 2007.
- [13] A. Kapoor, M. Li, and R. Taylor, "Spatial motion constraints for robot assisted suturing using virtual fixtures," in *Medical Image Computing And Computer-Assisted Intervention (MICCAI'05)*, vol. 3750, 2005, pp. 89–96.
- [14] P. Marayong, M. Li, A. Okamura, and G. Hager, "Spatial motion constraints: Theory and demonstrations for robot guidance using virtual fixtures," in *Proceedings of the 2003 IEEE International Conference On Robotics And Automation*, 2003, pp. 1954–1959.
- [15] L. B. Rosenberg, "Virtual fixtures: Perceptual tools for telerobotic manipulation," in *IEEE Virtual Reality Annual International Symposium*, 1993, pp. 76–82.
- [16] H. Wang, S. Wang, J. Ding, and H. Luo, "Suturing and tying knots assisted by a surgical robot system in laryngeal mis," *Robotica*, vol. 28, pp. 241–252, March 2010.
- [17] B. Brehmer, C. Moll, A. Markis, R. Kirschner-Hermanis, R. Knüchel, and G. Jakse, "Endosew: A new device for laparoscopic running sutures," *Journal Of Endourology*, vol. 22, pp. 307–311, February 2008.
- [18] T. Göpel, F. Haärtl, A. Schneider, M. Buss, and H. Feussner, "Automation of a suturing device for minimally invasive surgery," *Surgical Endoscopy*, vol. 25, pp. 2100–2104, July 2011.
- [19] J. F. Kuniholm, G. D. Buckner, W. Nifong, and M. Orrico, "Automated knot tying for fixation in minimally invasive, robot-assisted cardiac surgery," *Journal of Biomechanical Engineering*, vol. 127, pp. 1001–1008, 2005.
- [20] R. Bauernschmitt, E. U. Schirmbeck, A. Knoll, H. Mayer, I. Nagy, N. Wessel, S. M. Wildhirt, and R. Lange, "Towards robotic heart surgery: Introduction of autonomous procedures into an experimental surgical telemanipulator system," *The International Journal of Medical Robotics and Computer Assisted Surgery*, vol. 1, pp. 74–79, 2005.
- [21] H. Kang and J. T. Wen, "Robotic assistants aid surgeons during minimally invasive procedures," *IEEE Engineering in Medicine and Biology*, vol. 20, no. 1, pp. 94–104, 2001.
- [22] S. Iyer, T. Looi, and J. Drake, "A single arm, single camera system for automated suturing," in *Proceedings of the IEEE 2013 International Conference on Robotics and Automation (ICRA'13)*, 2013.
- [23] C. Staub, T. Osa, A. Knoll, and R. Bauernschmitt, "Automation of tissue piercing using circular needles and vision guidance for computer aided laparoscopic surgery," in *Proceedings of the IEEE 2010 International Conference on Robotics and Automation (ICRA'10)*, 2010.
- [24] C. E. Reiley, E. Plaku, and G. D. Hager, "Motion generation of robotic surgical tasks: Learning from expert demonstrations," in *32nd Annual International Conference of the IEEE Engineering in Medicine and Biology Society (EMBC)*, Sept 2010.
- [25] S. L. Troyan, V. Kianzad, S. L. Gibbs-Strauss, S. Gioux, A. Matsuiand, R. Oketokoun, L. Ngo, A. Khamene, F. Azar, and J. V. Frangioni, "The FLARE™ intraoperative near-infrared fluorescence imaging system: A first-in-human clinical trial in breast cancer sentinel lymph node mapping," *Annals of Surgical Oncology*, vol. 16, pp. 2943–2952, 2009.
- [26] J. V. Frangioni, "In vivo near-infrared fluorescence imaging," *Current Opinion in Chemical Biology*, vol. 7, pp. 626–634, 2003.
- [27] R. Hartley and A. Zisserman, *Multiple View Geometry in Computer Vision*. Cambridge University Press, 2003.
- [28] K. Arun, T. Huang, and S. Blostein, "Least-squares fitting of two 3-d point sets," *IEEE Transactions on Pattern Analysis and Machine Intelligence*, vol. 9, no. 5, pp. 698–700, September 1987.